Search for heavy metastable particles decaying to jet pairs in $p\bar{p}$ collisions at $\sqrt{s} = 1.96$ TeV

T. Aaltonen,[21] B. Álvarez González,[9,w] S. Amerio,[41a] D. Amidei,[32] A. Anastassov,[36] A. Annovi,[17] J. Antos,[12] G. Apollinari,[15] J. A. Appel,[15] A. Apresyan,[46] T. Arisawa,[56] A. Artikov,[13] J. Asaadi,[51] W. Ashmanskas,[15] B. Auerbach,[59] A. Aurisano,[51] F. Azfar,[40] W. Badgett,[15] A. Barbaro-Galtieri,[26] V. E. Barnes,[46] B. A. Barnett,[23] P. Barria,[44a,44c] P. Bartos,[12] M. Bauce,[41a,41b] G. Bauer,[30] F. Bedeschi,[44a] D. Beecher,[28] S. Behari,[23] G. Bellettini,[44a,44b] J. Bellinger,[58] D. Benjamin,[14] A. Beretvas,[15] A. Bhatti,[48] M. Binkley,[15,a] D. Bisello,[41a,41b] I. Bizjak,[28,aa] K. R. Bland,[5] B. Blumenfeld,[23] A. Bocci,[14] A. Bodek,[47] D. Bortoletto,[46] J. Boudreau,[45] A. Boveia,[11] B. Brau,[15,b] L. Brigliadori,[6a,6b] A. Brisuda,[12] C. Bromberg,[33] E. Brucken,[21] M. Bucciantonio,[44a,44b] J. Budagov,[13] H. S. Budd,[47] S. Budd,[22] K. Burkett,[15] G. Busetto,[41a,41b] P. Bussey,[19] A. Buzatu,[31] C. Calancha,[29] S. Camarda,[4] M. Campanelli,[33] M. Campbell,[32] F. Canelli,[12,15] A. Canepa,[43] B. Carls,[22] D. Carlsmith,[58] R. Carosi,[44a] S. Carrillo,[16,l] S. Carron,[15] B. Casal,[9] M. Casarsa,[15] A. Castro,[6a,6b] P. Catastini,[15] D. Cauz,[52a] V. Cavaliere,[44a,44c] M. Cavalli-Sforza,[4] A. Cerri,[26,g] L. Cerrito,[28,r] Y. C. Chen,[1] M. Chertok,[7] G. Chiarelli,[44a] G. Chlachidze,[15] F. Chlebana,[15] K. Cho,[25] D. Chokheli,[13] J. P. Chou,[20] W. H. Chung,[58] Y. S. Chung,[47] C. I. Ciobanu,[42] M. A. Ciocci,[44a,44c] A. Clark,[18] G. Compostella,[41a,41b] M. E. Convery,[15] J. Conway,[7] M. Corbo,[42] M. Cordelli,[17] C. A. Cox,[7] D. J. Cox,[7] F. Crescioli,[44a,44b] C. Cuenca Almenar,[59] J. Cuevas,[9,w] R. Culbertson,[15] D. Dagenhart,[15] N. d'Ascenzo,[42,u] M. Datta,[15] P. de Barbaro,[47] S. De Cecco,[49a] G. De Lorenzo,[4] M. Dell'Orso,[44a,44b] C. Deluca,[4] L. Demortier,[48] J. Deng,[14,d] M. Deninno,[6a] F. Devoto,[21] M. d'Errico,[41a,41b] A. Di Canto,[44a,44b] B. Di Ruzza,[44a] J. R. Dittmann,[5] M. D'Onofrio,[27] S. Donati,[44a,44b] P. Dong,[15] M. Dorigo,[52a] T. Dorigo,[41a] K. Ebina,[56] A. Elagin,[51] A. Eppig,[32] R. Erbacher,[7] D. Errede,[22] S. Errede,[22] N. Ershaidat,[42,z] R. Eusebi,[51] H. C. Fang,[26] S. Farrington,[40] M. Feindt,[24] J. P. Fernandez,[29] C. Ferrazza,[44a,44d] R. Field,[16] G. Flanagan,[46,s] R. Forrest,[7] M. J. Frank,[5] M. Franklin,[20] J. C. Freeman,[15] Y. Funakoshi,[56] I. Furic,[16] M. Gallinaro,[48] J. Galyardt,[10] J. E. Garcia,[18] A. F. Garfinkel,[46] P. Garosi,[44a,44c] H. Gerberich,[22] E. Gerchtein,[15] S. Giagu,[49a,49b] V. Giakoumopoulou,[3] P. Giannetti,[44a] K. Gibson,[45] C. M. Ginsburg,[15] N. Giokaris,[3] P. Giromini,[17] M. Giunta,[44a] G. Giurgiu,[23] V. Glagolev,[13] D. Glenzinski,[15] M. Gold,[35] D. Goldin,[51] N. Goldschmidt,[16] A. Golossanov,[15] G. Gomez,[9] G. Gomez-Ceballos,[30] M. Goncharov,[30] O. González,[29] I. Gorelov,[35] A. T. Goshaw,[14] K. Goulianos,[48] A. Gresele,[41a] S. Grinstein,[4] C. Grosso-Pilcher,[11] R. C. Group,[55] J. Guimaraes da Costa,[20] Z. Gunay-Unalan,[33] C. Haber,[26] S. R. Hahn,[15] E. Halkiadakis,[50] A. Hamaguchi,[39] J. Y. Han,[47] F. Happacher,[17] K. Hara,[53] D. Hare,[50] M. Hare,[54] R. F. Harr,[57] K. Hatakeyama,[5] C. Hays,[40] M. Heck,[24] J. Heinrich,[43] M. Herndon,[58] S. Hewamanage,[5] D. Hidas,[50] A. Hocker,[15] W. Hopkins,[15,h] D. Horn,[24] S. Hou,[1] R. E. Hughes,[37] M. Hurwitz,[11] U. Husemann,[59] N. Hussain,[31] M. Hussein,[33] J. Huston,[33] G. Introzzi,[44a] M. Iori,[49a,49b] A. Ivanov,[7,p] E. James,[15] D. Jang,[10] B. Jayatilaka,[14] E. J. Jeon,[25] M. K. Jha,[6a] S. Jindariani,[15] W. Johnson,[7] M. Jones,[46] K. K. Joo,[25] S. Y. Jun,[10] T. R. Junk,[15] T. Kamon,[51] P. E. Karchin,[57] Y. Kato,[39,o] W. Ketchum,[11] J. Keung,[43] V. Khotilovich,[51] B. Kilminster,[15] D. H. Kim,[25] H. S. Kim,[25] H. W. Kim,[25] J. E. Kim,[25] M. J. Kim,[17] S. B. Kim,[25] S. H. Kim,[53] Y. K. Kim,[11] N. Kimura,[56] M. Kirby,[15] S. Klimenko,[16] K. Kondo,[56] D. J. Kong,[25] J. Konigsberg,[16] A. V. Kotwal,[14] M. Kreps,[24] J. Kroll,[43] D. Krop,[11] N. Krumnack,[5,m] M. Kruse,[14] V. Krutelyov,[51,e] T. Kuhr,[24] M. Kurata,[53] S. Kwang,[11] A. T. Laasanen,[46] S. Lami,[44a] S. Lammel,[15] M. Lancaster,[28] R. L. Lander,[7] K. Lannon,[37,v] A. Lath,[50] G. Latino,[44a,44c] I. Lazzizzera,[41a] T. LeCompte,[2] E. Lee,[51] H. S. Lee,[11] J. S. Lee,[25] S. W. Lee,[51,x] S. Leo,[44a,44b] S. Leone,[44a] J. D. Lewis,[15] C.-J. Lin,[26] J. Linacre,[40] M. Lindgren,[15] E. Lipeles,[43] A. Lister,[18] D. O. Litvintsev,[15] C. Liu,[45] Q. Liu,[46] T. Liu,[15] S. Lockwitz,[59] N. S. Lockyer,[43] A. Loginov,[59] D. Lucchesi,[41a,41b] J. Lueck,[24] P. Lujan,[26] P. Lukens,[15] G. Lungu,[48] J. Lys,[26] R. Lysak,[12] R. Madrak,[15] K. Maeshima,[15] K. Makhoul,[30] P. Maksimovic,[23] S. Malik,[48] G. Manca,[27,c] A. Manousakis-Katsikakis,[3] F. Margaroli,[46] C. Marino,[24] M. Martínez,[4] R. Martínez-Ballarín,[29] P. Mastrandrea,[49a] M. Mathis,[23] M. E. Mattson,[57] P. Mazzanti,[6a] K. S. McFarland,[47] P. McIntyre,[51] R. McNulty,[27,j] A. Mehta,[27] P. Mehtala,[21] A. Menzione,[44a] C. Mesropian,[48] T. Miao,[15] D. Mietlicki,[32] A. Mitra,[1] H. Miyake,[53] S. Moed,[20] N. Moggi,[6a] M. N. Mondragon,[15,l] C. S. Moon,[25] R. Moore,[15] M. J. Morello,[15] J. Morlock,[24] P. Movilla Fernandez,[15] A. Mukherjee,[15] Th. Muller,[24] P. Murat,[15] M. Mussini,[6a,6b] J. Nachtman,[15,n] Y. Nagai,[53] J. Naganoma,[56] I. Nakano,[38] A. Napier,[54] J. Nett,[51] C. Neu,[55] M. S. Neubauer,[22] J. Nielsen,[26,f] L. Nodulman,[2] O. Norniella,[22] E. Nurse,[28] L. Oakes,[40] S. H. Oh,[14] Y. D. Oh,[25] I. Oksuzian,[55] T. Okusawa,[39] R. Orava,[21] L. Ortolan,[4] S. Pagan Griso,[41a,41b] C. Pagliarone,[52a] E. Palencia,[9,g] V. Papadimitriou,[15] A. A. Paramonov,[2] J. Patrick,[15] G. Pauletta,[52a,52b] M. Paulini,[10] C. Paus,[30] D. E. Pellett,[7] A. Penzo,[52a] T. J. Phillips,[14] G. Piacentino,[44a] E. Pianori,[43] J. Pilot,[37] K. Pitts,[22] C. Plager,[8] L. Pondrom,[58] K. Potamianos,[46] O. Poukhov,[13,a] F. Prokoshin,[13,y] A. Pronko,[15] F. Ptohos,[17,i] E. Pueschel,[10] G. Punzi,[44a,44b] J. Pursley,[58] A. Rahaman,[45] V. Ramakrishnan,[58] N. Ranjan,[46] I. Redondo,[29] P. Renton,[40] M. Rescigno,[49a] F. Rimondi,[6a,6b] L. Ristori,[45,15] A. Robson,[19] T. Rodrigo,[9] T. Rodriguez,[43] E. Rogers,[22] S. Rolli,[54] R. Roser,[15] M. Rossi,[52a] F. Rubbo,[15] F. Ruffini,[44a,44c] A. Ruiz,[9] J. Russ,[10] V. Rusu,[15] A. Safonov,[51]

W. K. Sakumoto,[47] Y. Sakurai,[56] L. Santi,[52a,52b] L. Sartori,[44a] K. Sato,[53] V. Saveliev,[42,u] A. Savoy-Navarro,[42] P. Schlabach,[15] A. Schmidt,[24] E. E. Schmidt,[15] M. P. Schmidt,[59,a] M. Schmitt,[36] T. Schwarz,[7] L. Scodellaro,[9] A. Scribano,[44a,44c] F. Scuri,[44a] A. Sedov,[46] S. Seidel,[35] Y. Seiya,[39] A. Semenov,[13] F. Sforza,[44a,44b] A. Sfyrla,[22] S. Z. Shalhout,[7] T. Shears,[27] P. F. Shepard,[45] M. Shimojima,[53,t] S. Shiraishi,[11] M. Shochet,[11] I. Shreyber,[34] A. Simonenko,[13] P. Sinervo,[31] A. Sissakian,[13,a] K. Sliwa,[54] J. R. Smith,[7] F. D. Snider,[15] A. Soha,[15] S. Somalwar,[50] V. Sorin,[4] P. Squillacioti,[15] M. Stancari,[15] M. Stanitzki,[59] R. St. Denis,[19] B. Stelzer,[31] O. Stelzer-Chilton,[31] D. Stentz,[36] J. Strologas,[35] G. L. Strycker,[32] Y. Sudo,[53] A. Sukhanov,[16] I. Suslov,[13] K. Takemasa,[53] Y. Takeuchi,[53] J. Tang,[11] M. Tecchio,[32] P. K. Teng,[1] J. Thom,[15,h] J. Thome,[10] G. A. Thompson,[22] E. Thomson,[43] P. Ttito-Guzmán,[29] S. Tkaczyk,[15] D. Toback,[51] S. Tokar,[12] K. Tollefson,[33] T. Tomura,[53] D. Tonelli,[15] S. Torre,[17] D. Torretta,[15] P. Totaro,[52a,52b] M. Trovato,[44a,44d] Y. Tu,[43] F. Ukegawa,[53] S. Uozumi,[25] A. Varganov,[32] F. Vázquez,[16,l] G. Velev,[15] C. Vellidis,[3] M. Vidal,[29] I. Vila,[9] R. Vilar,[9] J. Vizán,[9] M. Vogel,[35] G. Volpi,[44a,44b] P. Wagner,[43] R. L. Wagner,[15] T. Wakisaka,[39] R. Wallny,[8] S. M. Wang,[1] A. Warburton,[31] D. Waters,[28] M. Weinberger,[51] W. C. Wester III,[15] B. Whitehouse,[54] D. Whiteson,[43,d] A. B. Wicklund,[2] E. Wicklund,[15] S. Wilbur,[11] F. Wick,[24] H. H. Williams,[43] J. S. Wilson,[37] P. Wilson,[15] B. L. Winer,[37] P. Wittich,[15,h] S. Wolbers,[15] H. Wolfe,[37] T. Wright,[32] X. Wu,[18] Z. Wu,[5] K. Yamamoto,[39] J. Yamaoka,[14] T. Yang,[15] U. K. Yang,[11,q] Y. C. Yang,[25] W.-M. Yao,[26] G. P. Yeh,[15] K. Yi,[15,n] J. Yoh,[15] K. Yorita,[56] T. Yoshida,[39,k] G. B. Yu,[14] I. Yu,[25] S. S. Yu,[15] J. C. Yun,[15] A. Zanetti,[52a] Y. Zeng,[14] and S. Zucchelli[6a,6b]

(CDF Collaboration)

[1]*Institute of Physics, Academia Sinica, Taipei, Taiwan 11529, Republic of China*
[2]*Argonne National Laboratory, Argonne, Illinois 60439, USA*
[3]*University of Athens, 157 71 Athens, Greece*
[4]*Institut de Fisica d'Altes Energies, ICREA, Universitat Autonoma de Barcelona, E-08193, Bellaterra (Barcelona), Spain*
[5]*Baylor University, Waco, Texas 76798, USA*
[6a]*Istituto Nazionale di Fisica Nucleare Bologna, I-40127 Bologna, Italy*
[6b]*University of Bologna, I-40127 Bologna, Italy*
[7]*University of California, Davis, Davis, California 95616, USA*
[8]*University of California, Los Angeles, Los Angeles, California 90024, USA*
[9]*Instituto de Fisica de Cantabria, CSIC-University of Cantabria, 39005 Santander, Spain*
[10]*Carnegie Mellon University, Pittsburgh, Pennsylvania 15213, USA*
[11]*Enrico Fermi Institute, University of Chicago, Chicago, Illinois 60637, USA*
[12]*Comenius University, 842 48 Bratislava, Slovakia; Institute of Experimental Physics, 040 01 Kosice, Slovakia*
[13]*Joint Institute for Nuclear Research, RU-141980 Dubna, Russia*
[14]*Duke University, Durham, North Carolina 27708, USA*
[15]*Fermi National Accelerator Laboratory, Batavia, Illinois 60510, USA*
[16]*University of Florida, Gainesville, Florida 32611, USA*
[17]*Laboratori Nazionali di Frascati, Istituto Nazionale di Fisica Nucleare, I-00044 Frascati, Italy*
[18]*University of Geneva, CH-1211 Geneva 4, Switzerland*
[19]*Glasgow University, Glasgow G12 8QQ, United Kingdom*
[20]*Harvard University, Cambridge, Massachusetts 02138, USA*
[21]*Division of High Energy Physics, Department of Physics, University of Helsinki and Helsinki Institute of Physics, FIN-00014, Helsinki, Finland*
[22]*University of Illinois, Urbana, Illinois 61801, USA*
[23]*The Johns Hopkins University, Baltimore, Maryland 21218, USA*
[24]*Institut für Experimentelle Kernphysik, Karlsruhe Institute of Technology, D-76131 Karlsruhe, Germany*
[25]*Center for High Energy Physics: Kyungpook National University, Daegu 702-701, Korea; Seoul National University, Seoul 151-742, Korea; Sungkyunkwan University, Suwon 440-746, Korea; Korea Institute of Science and Technology Information, Daejeon 305-806, Korea; Chonnam National University, Gwangju 500-757, Korea; Chonbuk National University, Jeonju 561-756, Korea*
[26]*Ernest Orlando Lawrence Berkeley National Laboratory, Berkeley, California 94720, USA*
[27]*University of Liverpool, Liverpool L69 7ZE, United Kingdom*
[28]*University College London, London WC1E 6BT, United Kingdom*
[29]*Centro de Investigaciones Energeticas Medioambientales y Tecnologicas, E-28040 Madrid, Spain*
[30]*Massachusetts Institute of Technology, Cambridge, Massachusetts 02139, USA*
[31]*Institute of Particle Physics: McGill University, Montréal, Québec, Canada H3A 2T8; Simon Fraser University, Burnaby, British Columbia, Canada V5A 1S6; University of Toronto, Toronto, Ontario, Canada M5S 1A7; and TRIUMF, Vancouver, British Columbia, Canada V6T 2A3*

[32]*University of Michigan, Ann Arbor, Michigan 48109, USA*
[33]*Michigan State University, East Lansing, Michigan 48824, USA*
[34]*Institution for Theoretical and Experimental Physics, ITEP, Moscow 117259, Russia*
[35]*University of New Mexico, Albuquerque, New Mexico 87131, USA*
[36]*Northwestern University, Evanston, Illinois 60208, USA*
[37]*The Ohio State University, Columbus, Ohio 43210, USA*
[38]*Okayama University, Okayama 700-8530, Japan*
[39]*Osaka City University, Osaka 588, Japan*
[40]*University of Oxford, Oxford OX1 3RH, United Kingdom*
[41a]*Istituto Nazionale di Fisica Nucleare, Sezione di Padova-Trento, Italy*
[41b]*University of Padova, I-35131 Padova, Italy*
[42]*LPNHE, Universite Pierre et Marie Curie/IN2P3-CNRS, UMR7585, Paris, F-75252 France*
[43]*University of Pennsylvania, Philadelphia, Pennsylvania 19104, USA*
[44a]*Istituto Nazionale di Fisica Nucleare Pisa, I-56127 Pisa Italy*
[44b]*University of Pisa, I-56127 Pisa, Italy*
[44c]*University of Siena, I-56127 Pisa, Italy*
[44d]*Scuola Normale Superiore, I-56127 Pisa, Italy*
[45]*University of Pittsburgh, Pittsburgh, Pennsylvania 15260, USA*
[46]*Purdue University, West Lafayette, Indiana 47907, USA*
[47]*University of Rochester, Rochester, New York 14627, USA*
[48]*The Rockefeller University, New York, New York 10065, USA*
[49a]*Istituto Nazionale di Fisica Nucleare, Sezione di Roma 1, I-00185 Roma, Italy*
[49b]*Sapienza Università di Roma, I-00185 Roma, Italy*
[50]*Rutgers University, Piscataway, New Jersey 08855, USA*
[51]*Texas A&M University, College Station, Texas 77843, USA*
[52a]*Istituto Nazionale di Fisica Nucleare Trieste/Udine, I-34100 Trieste, Italy*
[52b]*University of Trieste/Udine, I-33100 Udine, Italy*
[53]*University of Tsukuba, Tsukuba, Ibaraki 305, Japan*
[54]*Tufts University, Medford, Massachusetts 02155, USA*
[55]*University of Virginia, Charlottesville, Virginia 22906, USA*
[56]*Waseda University, Tokyo 169, Japan*
[57]*Wayne State University, Detroit, Michigan 48201, USA*

[a]Deceased
[b]Visitor from University of Massachusetts—Amherst, Amherst, MA 01003, USA.
[c]Visitor from Istituto Nazionale di Fisica Nucleare, Sezione di Cagliari, 09042 Monserrato (Cagliari), Italy.
[d]Visitor from University of California Irvine, Irvine, CA 92697, USA.
[e]Visitor from University of California Santa Barbara, Santa Barbara, CA 93106, USA.
[f]Visitor from University of California Santa Cruz, Santa Cruz, CA 95064, USA.
[g]Visitor from CERN,CH-1211 Geneva, Switzerland.
[h]Visitor from Cornell University, Ithaca, NY 14853, USA.
[i]Visitor from University of Cyprus, Nicosia CY-1678, Cyprus.
[j]Visitor from University College Dublin, Dublin 4, Ireland.
[k]Visitor from University of Fukui, Fukui City, Fukui Prefecture, Japan 910-0017.
[l]Visitor from Universidad Iberoamericana, Mexico D. F., Mexico.
[m]Visitor from Iowa State University, Ames, IA 50011, USA.
[n]Visitor from University of Iowa, Iowa City, IA 52242, USA.
[o]Visitor from Kinki University, Higashi-Osaka City, Japan 577-8502.
[p]Visitor from Kansas State University, Manhattan, KS 66506, USA.
[q]Visitor from University of Manchester, Manchester M13 9PL, England.
[r]Visitor from Queen Mary, University of London, London, E1 4NS, England.
[s]Visitor from Muons, Inc., Batavia, IL 60510, USA.
[t]Visitor from Nagasaki Institute of Applied Science, Nagasaki, Japan.
[u]Visitor from National Research Nuclear University, Moscow, Russia.
[v]Visitor from University of Notre Dame, Notre Dame, IN 46556, USA.
[w]Visitor from Universidad de Oviedo, E-33007 Oviedo, Spain.
[x]Visitor from Texas Tech University, Lubbock, TX 79609, USA.
[y]Visitor from Universidad Tecnica Federico Santa Maria, 110v Valparaiso, Chile.
[z]Visitor from Yarmouk University, Irbid 211-63, Jordan.
[aa]On leave from J. Stefan Institute, Ljubljana, Slovenia.

[58]*University of Wisconsin, Madison, Wisconsin 53706, USA*
[59]*Yale University, New Haven, Connecticut 06520, USA*
(Received 16 September 2011; published 24 January 2012)

A search is performed for heavy metastable particles that decay into jet pairs with a macroscopic lifetime ($c\tau \sim 1$ cm) in $p\bar{p}$ collisions at $\sqrt{s} = 1.96$ TeV using data from the CDF II detector at Fermilab corresponding to an integrated luminosity of 3.2 fb^{-1}. To estimate the standard model background, a data-driven approach is used. Probability-density functions are constructed to model secondary vertices from known processes. No statistically significant excess is observed above the background. Limits on the production cross section in a hidden valley benchmark phenomenology are set for various Higgs boson masses as well as metastable particle masses and lifetimes.

DOI: 10.1103/PhysRevD.85.012007 PACS numbers: 13.85.Ni, 12.60.Fr, 14.80.Da

I. INTRODUCTION

The standard model (SM) of elementary particles fails at TeV energies if no new phenomena appear at this scale. A single Higgs boson provides the simplest solution, but there are other possibilities, some of which predict massive metastable particles. They are metastable because they can only decay to SM particles through diagrams containing a new high-mass force carrier or a loop of very massive particles. These models are broadly categorized as ''hidden valley'' (HV) models [1]. We use data from $p\bar{p}$ collisions at $\sqrt{s} = 1.96$ TeV collected with the CDF II detector at the Fermilab Tevatron collider to search for a long-lived massive particle that originates from the primary $p\bar{p}$ interaction, travels a macroscopic distance (of order 1 cm), and decays into jet pairs. A variety of predicted decay modes are possible for these metastable particles. Although the search is sensitive to any massive long-lived particle decaying into jet pairs, for the sake of specificity, we choose as a benchmark to evaluate the results within the context of the HV phenomenology.

A recent analysis from the D0 experiment searched for heavy particles decaying with a displaced vertex [2], using the same phenomenological model as this analysis. However, it was restricted to heavy metastable particles that decay into b quarks because their trigger required a muon in the event. We have no such limitation because CDF employs the silicon vertex trigger (SVT) which allows us to trigger on tracks that originate from displaced vertices [3,4]. Thus, our search is sensitive to metastable particles that decay into any jets, not only b-quark jets.

We search for an event signature where two jets of particles emanate from a point displaced from the primary interaction point, *i.e.*, a displaced or secondary vertex. Monte Carlo (MC) simulation is used to model events from the HV phenomenology. It serves as our benchmark for processes containing the signature of the search. Since the SM does not contain massive metastable particles, we expect little background. We construct a background model almost entirely from the data. To accomplish this, the kinematics of the data events with secondary vertex characteristics are determined from auxiliary SM samples.

After a brief overview of the CDF II detector in Sec. II, the HV phenomenology is described in Sec. III. Section IV discusses the event selection for the analysis, and Sec. V presents the background estimate along with a test of the method. The search for the signal is presented in Sec. VI. Systematic uncertainties for both the expected signal and the background are presented in Sec. VII. Section VIII presents limits on the production cross-section in the HV phenomenology.

II. THE CDF DETECTOR

CDF is a general-purpose detector that is described in detail in Ref. [5]. The detector components relevant to this analysis are briefly described here. Closest to the beam pipe are multilayer silicon detectors (SVX) [6] providing precision tracking which is used to identify displaced vertices. Outside the multilayer silicon detectors is an open-cell drift chamber, the central outer tracker (COT), covering the pseudorapidity region $|\eta| < 1$ [7]. (The pseudorapidity η is defined as $-\ln[\tan(\theta/2)]$, where θ is the polar angle relative to the proton beam direction [8].) The COT is used to reconstruct charged particles' momenta. The tracking system is enclosed in a superconducting solenoid operating at 1.4 T, which in turn is surrounded by a calorimeter.

The CDF calorimeter system is separated into electromagnetic and hadronic components segmented in a projective tower geometry covering the region $|\eta| < 3.6$. The electromagnetic calorimeters use a lead-scintillator sampling technology [9], whereas the hadron calorimeters use iron-scintillator technology [10,11]. Jets are reconstructed from the energy deposited in these calorimeters [12]. The calorimeter is separated into the central ($|\eta| < 1.0$) and forward (or plug) regions ($|\eta| > 1.0$).

Finally, the muon subdetectors are arrayed outside the calorimeters. The beam luminosity is determined with gas Cherenkov counters located in the region $3.7 < |\eta| < 4.7$ which measure the average number of inelastic $p\bar{p}$ collisions per accelerator bunch crossing [13].

CDF uses a three-level trigger system, with a mix of hardware electronics and dedicated CPUs to select interesting events. In our analysis, a trigger sensitive to $Z \rightarrow b\bar{b}$

decays is used, the ZBB trigger. It employs the SVT hardware in the second-level trigger. This trigger is described in more detail in Sec. IV.

III. THE HIDDEN VALLEY MODEL

A. Phenomenology

While the analysis presented here is a search for any heavy particle that decays into a pair of jets at a displaced vertex, it is useful to have a benchmark model. The HV phenomenology provides a framework in which we can generate signal Monte Carlo samples, search for discriminants, optimize our search, and compare results. Results presented for this benchmark process can be used to constrain other models by accounting for the differences in the kinematic properties of the final state. Here, we present a brief outline of the HV picture.

In the HV scenario, the standard model gauge group G_{SM} is extended by a non-Abelian group G_v [1,14]. SM particles are neutral under G_v. Additionally, G_v contains new particles, called v-particles, that are charged under G_v but neutral under G_{SM}.

In the particular class of hidden valley models considered here, the G_v gauge group may become strong and confine, analogously to QCD. The v-particles, called v-quarks in this class of models, are confined inside v-hadrons. Energetic collisions at the Tevatron could create new particles, such as the Higgs boson or a new Z' resonance, that could decay to HV particles. If the lightest v-hadrons are sufficiently heavy, they can decay to SM particles via highly suppressed processes, e.g., mixing with the longitudinal component of a Z'. A wide range of masses, lifetimes, and final states are possible within the HV framework. If the lightest available HV particle, a $v - \pi$ in our benchmark model, has mass less than twice that of the top quark, the predominant decay would be to $b\bar{b}$ quark pairs. With a long lifetime, some particles would travel a measurable distance from the primary vertex before decaying, much like a B or D hadron.

Applying the HV phenomenology to astroparticle physics, the authors in Ref. [15] theorize that the existence of a dark matter candidate implies another (HV) particle with a lifetime such that $c\tau$ is of the order of 1 cm. This places the lifetime within the range accessible to the CDF II detector.

The HV also provides a way to search for the Higgs boson. If the Higgs boson mixes with a scalar in the HV sector that couples to v-quarks, then it may decay to two (or more) v-hadrons. These v-hadrons would in turn decay into $b\bar{b}$ quark pairs. It would be feasible to search for the Higgs boson using this final state at CDF. Under some HV scenarios, the branching fraction to HV particles could be comparable to those of SM decays. In addition, searches for these HV decays may have higher signal-to-background ratios due to their unique decay topology. A Feynman diagram of this decay is shown in Fig. 1.

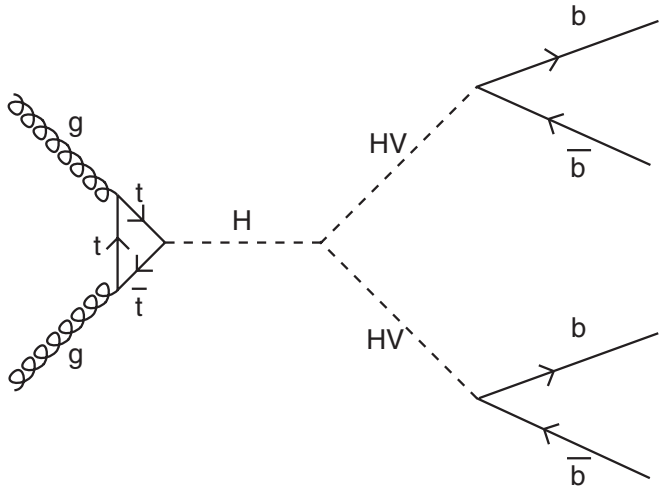

FIG. 1. Feynman diagram of Higgs boson production of a hidden valley particle and its subsequent decay. The coupling of HV particle to $b\bar{b}$ is extremely small, resulting in the long lifetime.

B. Monte Carlo Simulation Samples

The PYTHIA Monte Carlo program version 6.2 [16] is used to generate the events for the signal MC simulation. GEANT3 is used for the detector simulation [17]. To mimic HV production and decay in PYTHIA, we use the minimal supersymmetric standard model (MSSM) process of a CP-even Higgs boson (h^0) decaying into two CP-odd Higgs bosons (a^0) which in turn decay into b-quarks, $h^0 \rightarrow a^0 a^0 \rightarrow b\bar{b}b\bar{b}$. We alter the mass and lifetime of the a^0 in order to simulate the HV particle. This allows for the generation of signal MC samples using the PYTHIA MC generator without significant modification.

Two Higgs boson masses are generated, one at relatively low mass, 130 GeV/c^2, and one at higher mass, 170 GeV/c^2. Multiple HV particle masses from 20 GeV/c^2 to 65 GeV/c^2 are produced. The $c\tau$ of the HV particle, $c\tau_{\mathrm{HV}}$, is set to 1.0 cm. Some signal MC samples have been weighted to study HV particles with $c\tau_{\mathrm{HV}}$ of 0.3, 2.5, or 5.0 cm. Thus, we can study multiple HV lifetimes without generating additional signal MC samples.

C. Discriminants from signal MC simulation

The major characteristic that distinguishes the signal from the SM backgrounds is the presence of two jets whose momentum vectors both point to a common secondary vertex. With this in mind, we developed two discriminants shown in Figs. 2 and 3: ψ and ζ. In both cases, the figures are drawn in the two-dimensional plane transverse to the beam line.

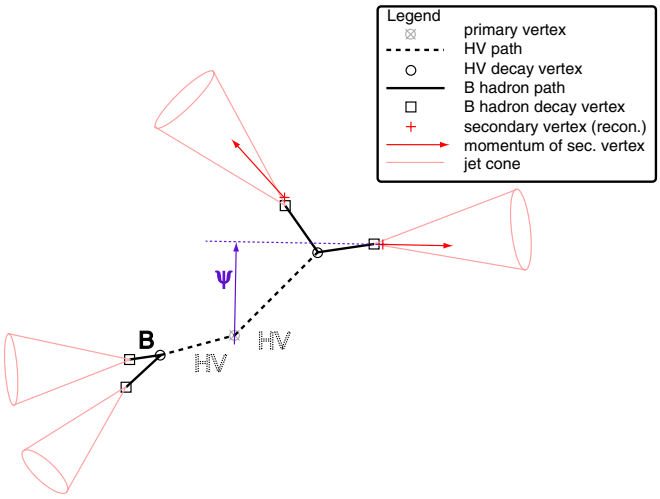

FIG. 2 (color online). Schematic diagram of variable ψ, the impact parameter of a jet with a secondary vertex. This figure is not to scale. The figure is shown in a plane transverse to the beam line.

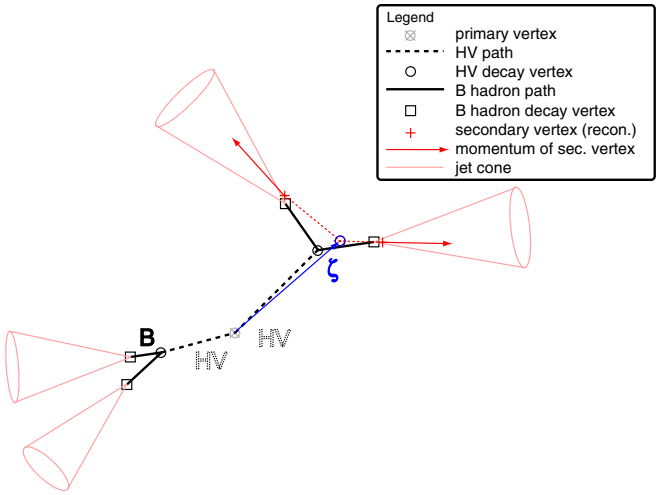

FIG. 3 (color online). Schematic diagram of variable $\vec{\zeta}$, which represents the decay vertex of the HV particle.

We define a "tagged jet" as a jet with a reconstructed secondary vertex using criteria defined in Sec. IV. By definition, such a jet has both a position (the secondary vertex) and a direction defined by the sum of momenta of the tracks that make up the vertex, where all these quantities are defined in the transverse plane. We define $\vec{\psi}$ as the orthogonal vector from the primary vertex, the reconstructed location of the $p\bar{p}$ collision, to the line defined by the secondary vertex position and momentum direction. The magnitude of $\vec{\psi}$ is the distance from the primary vertex to the line, *i.e.*, its impact parameter. We take the sign of ψ as that of the dot product between $\vec{\psi}$ and the momentum of the tagged jet. The distribution of ψ for simulated signal events has much larger tails than simulated background events.

The variable ζ is defined for events where there are two tagged jets; see Fig. 3. The intersection of the two-tag momenta can be thought of as the reconstructed decay vertex of the HV particle. The vector from the primary vertex to this reconstructed decay vertex is $\vec{\zeta}$; the magnitude, ζ, is the reconstructed two-dimensional decay distance of the HV particle.

The sign of ζ is determined by taking the dot product between $\vec{\zeta}$ and the vector sum of the momenta of the two jets with tags. The sign effectively indicates whether or not the decay vertex is in the same hemisphere of the detector as the jet pair. Signal MC events have more positive ζ than negative, while the background MC events have ζ uniformly distributed around zero.

At this point, it is necessary to discuss the combinatorics of the HV event topology. With MC simulation, we can use the generator-level information to evaluate if the jets with secondary vertices originated from quarks whose mother is the HV particle. Using this information, we define four possible topologies in which signal MC events can be classified.

(1) Two-tag HV: both jets originate from the *same* HV particle.
(2) One tag each: each jet originates from a different HV particle.
(3) One HV jet: one jet originates from a HV particle; the other does not.
(4) No HV jets: neither jet originates from a HV particle.

Figure 4 shows the (a) ψ and (b) ζ distributions for different signal MC simulation topologies and background MC simulation (PYTHIA QCD $b\bar{b}$). The signal MC assumes $M_H = 130$ GeV/c^2, $M_{\mathrm{HV}} = 40$ GeV/c^2, and $c\tau_{\mathrm{HV}} = 1.0$ cm. These distributions have been normalized to unit area and show the discriminating power of both variables.

For the two-tag-HV topology, the distribution of ζ is nearly always positive, which improves the discrimination against the background. The one-tag-each topology is a distribution that is both positive and negative, but mostly negative. Between the two-tag-HV and the one-tag-each topologies, we concern ourselves with the first because it has more discriminating power, and if a signal is seen, the HV particle's invariant mass can be reconstructed. The final two topologies are very rare, but are included in the figures for completeness.

In addition to these two variables, the separation of the two jets ($\Delta R = \sqrt{(\Delta\phi)^2 + (\Delta\eta)^2}$) is a useful discriminant (see Fig. 4(c)). In the two-tag-HV topology, the decay daughters of the HV particle are more collinear than the one-tag-each topology, but still different than the QCD background, which is dominated by gluon splitting at low ΔR, once a $\Delta R < 2.5$ cut removes most of the direct $b\bar{b}$ production.

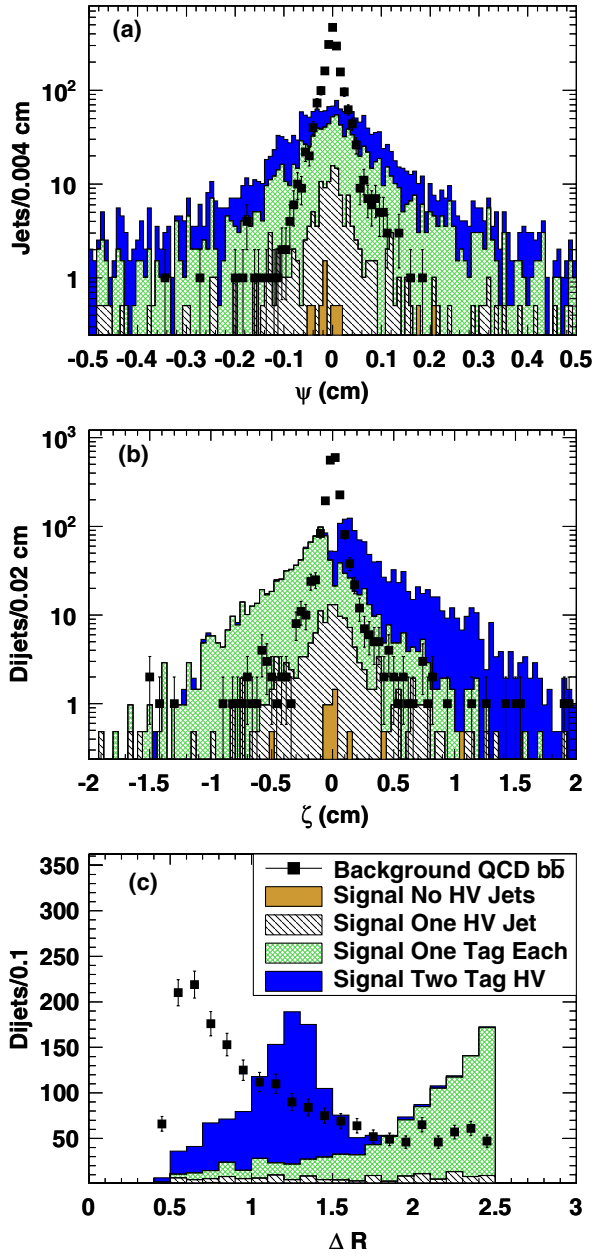

FIG. 4 (color online). Distributions of (a) ψ, (b) ζ, and (c) ΔR for dijets where both jets are tagged. The signal MC simulation histograms are stacked. In (a), only the leading jet of the jet pair is shown. In (c), a $\Delta R < 2.5$ cut has already been applied.

IV. EVENT SELECTION

A. ZBB trigger

$Z \rightarrow b\bar{b}$ events are collected at CDF for the purpose of studying the jet energy scale (JES) of b-quark jets [18,19]. This is achieved by means of a specially designed trigger, the ZBB trigger (Table I) which selects events containing tracks with a large impact parameter with respect to the primary vertex (d_0). Because a HV particle would decay at a displaced vertex, tracks from this decay would have large d_0. Thus, we use this trigger for our signal search. The total integrated luminosity collected with the ZBB trigger is 3.2 fb^{-1}.

At level 1, the trigger has two requirements. It selects events with at least one central calorimeter tower with $E_T > 5$ GeV and at least two tracks, one with $p_T > 5.48$ GeV/c, the other one with $p_T > 2.46$ GeV/c.

At level 2, there are two different paths, called opposite side (OS) and same side (SS), which refer to the topological configuration of the displaced tracks in the event. Both paths contain a veto on jets in the plug calorimeter and a central calorimeter requirement. The plug jet veto requires that there are no calorimeter clusters with $E_T > 5$ GeV in $|\eta| > 1.1$ and is designed to reduce the QCD background, which produces more gluon radiation than does the signal. The trigger requires at least two central calorimeter clusters, $E_T > 5$ GeV and $|\eta| < 1.1$, which are on opposite sides of the calorimeter. Finally, the calorimeter clusters must have in total at least two displaced SVT tracks, with track $p_T > 2$ GeV/c, $160\ \mu\text{m} < |d_0| < 1000\ \mu\text{m}$, secondary vertex fit $\chi^2 < 12$. For the OS path, the two tracks must have $150° < \Delta\phi < 180°$. The SS path requires that the two displaced tracks point to a single cluster, and that $2° < \Delta\phi < 30°$.

At level 3, the trigger requires at least two jets with $E_T > 10$ GeV and $|\eta| < 1.1$. Jet clustering uses a cone algorithm of size $\Delta R = 0.7$. The trigger also requires at least two tracks with $160\ \mu\text{m} < |d_0| < 1000\ \mu\text{m}$, to confirm the level-2 requirements. As a cross-check, this requirement is performed with both SVT tracks and COT tracks, with additional impact parameter significance and $|\Delta z|$ requirements imposed on the COT tracks. The track parameter z_0 is the distance in the z direction from the detector origin to the point on the z axis closest to the track helix. The quantity $|\Delta z|$ is the magnitude of the difference in z_0 between the two COT tracks. The cut on $|\Delta z|$ ensures both tracks originate from the same primary vertex. The same level-3 requirements are imposed on both OS and SS level-2 paths.

After the trigger selection, there is a further jet classification. Jets in the analysis stage are reconstructed with a $\Delta R = 0.4$ cone. The larger radius jet cone used in the trigger provides high trigger efficiency. In the analysis, a cone of 0.4 is used to avoid unnecessary merging of jets. The E_T of the jet, after being corrected to the hadron scale (E_T^{cor}) must be greater than 20 GeV. The jets must be in the central region of the detector, $|\eta| < 1.0$. This requirement overlaps with the ZBB trigger requirement. These jets are referred to as "tight-central" jets. However, as explained below, there are instances where non-tight-central jets are used in this analysis.

B. Signal and control regions

While the HV phenomenology predicts four jets in the final state, we allow events with three jets in order to increase our acceptance. In addition, the plug jet veto in

TABLE I. ZBB trigger requirements. One of the two level-2 paths, opposite side or same side must be satisfied.

Level 1	at least one central calorimeter tower with $E_T > 5$ GeV; at least two tracks: one track with $p_T > 5.48$ GeV/c, one with $p_T > 2.46$ GeV/c
Level 2	veto events with a calorimeter cluster with $E_T > 5$ GeV, $1.1 < \lvert\eta\rvert < 3.6$; require at least two clusters $E_T > 5$ GeV, $\lvert\eta\rvert < 1.1$, which have $135 < \Delta\phi < 180$; at least two SVT tracks with $p_T > 2$ GeV/c, 160 μm $< \lvert d_0\rvert < 1000$ μm, $\chi^2 < 12$
(OS)	tracks have $150° < \Delta\phi < 180°$
(SS)	tracks have $2° < \Delta\phi < 30°$
Level 3	at least two $\Delta R = 0.7$ jets with $E_T > 10$ GeV, $\lvert\eta\rvert < 1.1$; at least two SVT tracks with $p_T > 2$ GeV/c, $\lvert\eta\rvert < 1.2$, 160 μm $< \lvert d_0\rvert < 1000$ μm; at least two COT tracks with $p_T > 1.5$ GeV/c $\lvert\eta\rvert < 1.2$, 130 μm $< \lvert d_0\rvert < 1000$ μm, track impact parameter significance $S(d_0) > 3$, $\lvert\Delta z\rvert < 5$ cm

the ZBB trigger at level 2 reduces jet multiplicity (while simultaneously lowering the trigger rate at high luminosity). Thus, in order to maintain acceptance, the signal region is defined with three or more tight-central jets.

The signal MC samples show that the opening angle between the two jets is not back-to-back, but instead usually smaller. The lighter the HV particle, the smaller the opening angle between the jets. Thus, for each jet pair in a 3-or-more jet event, we apply a cut of $\Delta R < 2.5$ on each pair. Events which pass the jet multiplicity cut and have a jet pair passing the ΔR cut are said be in the signal region.

In addition to the signal region, we define a two-jet control region to validate our background estimation technique on a set of events that is devoid of signal. This control region is defined as follows: events are required to have exactly two tight-central jets with no ΔR requirement, and if additional jets are present, they must have uncorrected $E_T < 15$ GeV. The control and signal regions are mutually exclusive.

C. Secondary vertex tagging

Secondary vertex tagging is used in this analysis to identify jets with displaced vertices. We modified the standard CDF algorithm SECVTX [20] to increase the efficiency for very long-lived particles, such as the HV particle, by extending the maximum impact parameter allowed for tracks used in vertexing. Twenty $|d_0|_{\max}$ cuts between 0.15 cm and 1.6 cm are studied to maximize the signal while minimizing the increase in mistags. (Mistags are light-flavor quark or gluon jets erroneously tagged as having a displaced vertex.)

V. BACKGROUND ESTIMATION

We want to produce a background estimate that retains the kinematic correlations in QCD multijet events but has secondary vertices modeled on those observed in SM processes. Toward this end, we use the jet kinematics of our primary data sample, and to each event, we add secondary vertices whose properties come from other data samples. The vertices in these samples are characterized by probability-density functions (PDFs) as a function of jet energy, flavor, and the number of displaced tracks available to the ZBB trigger.

The ability to find particles with displaced vertices relies on the reconstruction of secondary vertices. These secondary vertices can come from multiple SM sources, which are listed in Table II.

A. Building PDFs

The first step in modeling the background is to build the standard model secondary vertex PDFs in tagged jets. The PDFs are constructed from data events, when possible, where the signal is not expected to be present, and in effect encapsulate SM secondary vertex information.

The PDF variables are defined in the plane transverse to the beam line. We define the variables for the secondary vertex with respect to the parent jet momentum vector, also called the jet axis. First, define $\vec{L}_{xy}$ as the two-dimensional vector from the primary vertex to the secondary vertex. There are two components to this $\vec{L}_{xy}$ vector, one parallel to the jet axis, one perpendicular. These two components are the first two PDF variables and are named u and v. These two variables define the position of a secondary vertex with respect to a jet axis.

The two-dimensional $\Delta\phi$ angle between the jet axis and the secondary vertex momentum vector is the third PDF variable, named α. This variable defines the direction of a secondary vertex with respect to a jet axis in the plane transverse to the beam.

We find that correlations exist among all three variables. To preserve these correlations, we store these PDFs in three-dimensional histograms.

TABLE II. Standard model processes that can result in jets with reconstructed displaced vertices.

Background	SM Production
b-quarks	QCD $b\bar{b}$, $t\bar{t}$, W/Z + jets, WZ/ZZ
c-quarks	QCD $c\bar{c}$, W/Z + jet, WZ/ZZ
light-flavor (mistags)	QCD $q\bar{q}$ & gg, hadronic τs

We split these PDFs into three main categories for different quark flavors: b-quark, c-quark, and light-flavor jets. These are further split into different bins of E_T^{cor} and the number of SVT tracks satisfying the ZBB-trigger SVT requirement. We separate jets into bins of zero, one, and two or more SVT tracks, as the ZBB trigger requires two displaced tracks in the event. We choose this binning because the PDFs' shapes are different in each bin, due to the dependence of secondary vertex production on these quantities.

Different data sources are used to construct the different quark flavor PDFs. We use a muon trigger with a relatively low p_T requirement to build the b-quark PDFs. These data are rich in B hadrons which decay semileptonically. To select events, we use a two-jet selection where one jet is required to have a muon present within its jet cone, and both jets are tagged while being well-separated in the detector ($\Delta\phi > 2.0$). The nonmuon jet, called the away jet, is the jet used to construct the b-quark PDFs.

For the light-flavor PDFs, we use the various CDF QCD jet triggers which collect a large number of QCD multijet data events. These data must have their heavy flavor contribution subtracted in order to isolate the light-flavor events with secondary vertices; in effect, these are mistag PDFs. The flavor composition of the jet triggers is calculated using QCD MC templates of b-quark, c-quark, and light-flavor secondary vertices. (In general, we refer to the secondary vertex modeling derived from data as PDFs, while reserving the word "template" to describe information obtained from MC samples.) PYTHIA QCD MC samples were generated with multiple momentum thresholds. The two samples we used in this analysis are QCD to $b\bar{b}$ and generalized QCD with no final-state filtering. The former is mostly used when comparing the signal MC in order to determine discriminants, see Sec. III. The latter is used to construct the MC templates for the purposes of estimating the background.

The vertex mass squared is the square of the sum of the four-momenta of the tracks that form the secondary vertex, where the mass of the track four-momentum is set to the mass of the pion. We determine the flavor composition of the jet trigger data by fitting the QCD MC templates of vertex mass to the data. Heavy flavor shapes (b- and c-quark contributions) are subtracted from the jet trigger data, using the QCD MC as the source of the shapes of the b- and c-quark distributions for u, v, and α.

In order to ensure that the b- and c-quark shapes for subtraction accurately represent the data, we compare the b-quark PDFs from the muon trigger to the QCD MC simulation where the jets are matched to a B hadron. The ratio of the means of each PDF variable is calculated as the scale factor. The shapes of the distributions of these variables are the same after applying these scale factors to the PDF variables for b-quark jets from the QCD MC simulation. These scale factors ($SF_u \sim 0.99$, $SF_v \sim 1.39$, $SF_\alpha \sim 1.04$) then are applied to the PDF variables for both b-quark and c-quark jets from the QCD MC simulation when generating the templates used in the subtraction procedure.

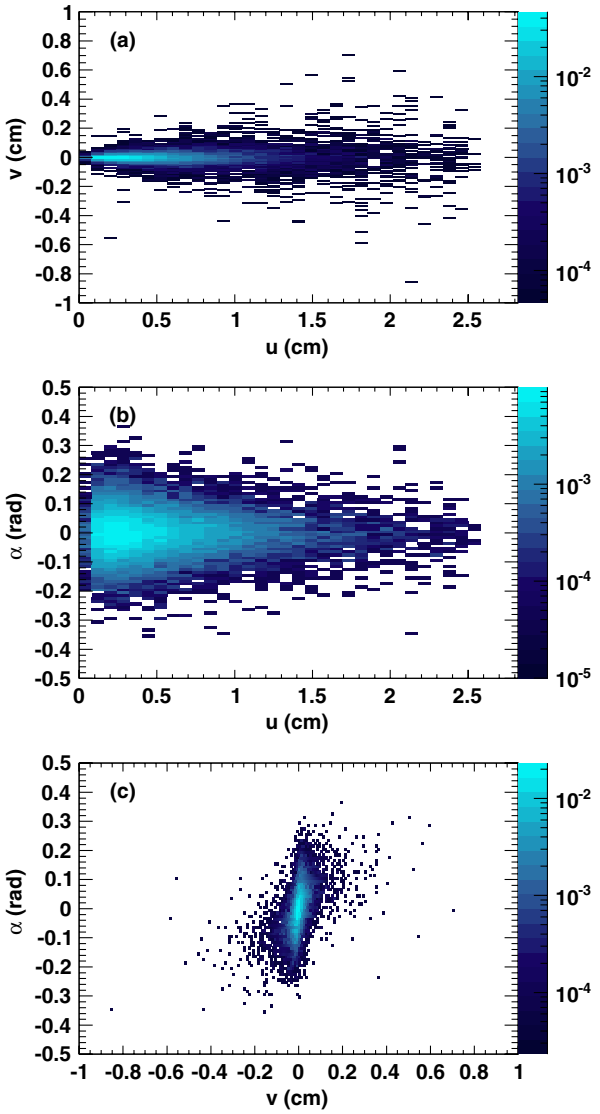

FIG. 5 (color online). Two-dimensional projections of a b-quark PDF for jets with E_T from 30 to 70 GeV and one SVT track within the jet: (a) u vs v, (b) α vs u, and (c) α vs v.

Finally, c-quark jets are not readily identifiable in real data. Therefore, we use QCD MC simulation in order to collect jets for the c-quark PDFs. This is not a serious limitation because we find that the ZBB data has a very small charm-quark component.

Two-dimensional projections of a b-quark PDF for jets with E_T from 30 to 70 GeV and one SVT track within the jet are shown in Fig. 5.

B. Pseudoevent generation

We build a background estimate using pseudoevents which are produced by applying the secondary vertex

PDFs to jets in events from the ZBB trigger data. While the kinematic information comes from the real event, the PDFs are used to characterize secondary vertices from SM sources in the jets.

The background estimate is done using the same ZBB trigger sample used to search for the signal. Events in the signal and control regions are separately selected. When generating pseudoevents, a pair of tight-central jets is used. For the signal region, this is the dijet system where $\Delta R < 2.5$. (In principle, there could be multiple dijets in a three-or-more-jet event, but in practice, we find only one dijet system in each event.) In the control region, the dijet system is simply the two tight-central jets in the event.

Before the pseudoevents are generated, we must understand the ZBB trigger data. First, we obtain the dijet tag probability of real dijets in the ZBB trigger data. This is the probability that *both* of the jets are tagged. The purpose of this dijet probability is to preserve kinematic correlations that may exist with respect to tagging. The dijet probability is calculated in terms of both the E_T of the jets and the number of SVT tracks, as the probability of a tag changes with these variables.

Second, we obtain the flavor composition of the dijets in the ZBB trigger data. However, unlike the flavor composition of the JET trigger samples, where we were concerned with single jets, here we are concerned with the flavor composition of pairs of jets. With three possible flavor categories: b-quark (B), c-quark (C), and light-flavor (L), and two jets, there are nine possible combinations of double flavors for a pseudodijet: BB, BC, BL, CB, CC, CL, LB, LC, and LL; where mixed states such as the BC and CB states are not considered degenerate. The first letter describes the flavor for the leading E_T jet and the second letter that of the subleading E_T jet.

We use two-dimensional fits of the vertex mass of the two vertices to determine the flavor of jet pairs with tags. We reuse the PYTHIA QCD dijet MC templates of the vertex mass. First, the individual b-quark, c-quark, and light-flavor MC templates are joined to form two-dimensional vertex mass templates for BB, BC, BL, etc. Then, the two-dimensional vertex mass templates are merged to form a single vertex mass template that encompasses all nine double-flavor states. Because the nine double-flavor fractions must add to one, there are eight fractions that we fit, which are algebraic combinations of the nine double-flavor states. Fits are performed using the ROOFIT package [21]; an example is shown in Fig. 6, and the fit result is shown in Table III.

The pseudoevent generation process is as follows: with a jet pair selected, from either the control region or signal region, we proceed to generate tags for the jets in the pair. The probability of both jets having tags, calculated from the ZBB data, is used to assign whether or not both jets have a tag in the pseudoevent.

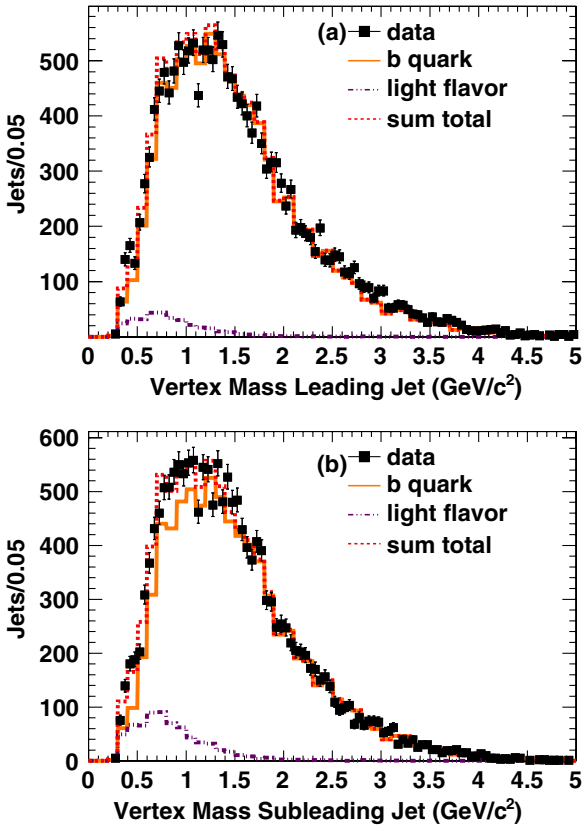

FIG. 6 (color online). Example of double-flavor fits for dijets where each jet has exactly one SVT trigger track. Histograms are projections of the two-dimensional fit onto the axis of each jet: (a) the higher E_T jet in the event, (b) the lower E_T jet.

Next, the flavor of the pseudojet is generated. Using Table III as an example, if both jets have exactly one SVT trigger track, there is a 91.28% probability that the jet pair is BB, or two b-quark jets, a 4.78% chance that the pair is BL, where the leading E_T jet is a b-quark jet and the subleading E_T jet is light-flavor, etc.

The secondary vertex information is sampled from the PDFs, generated using background processes. In this step, the jets are sampled independently. The sampling is

TABLE III. Double-flavor fraction fit results for dijets where each jet has exactly one SVT trigger track.

Double-Flavor State	(%)
BB	91.28 ± 0.96
BC	0 ± 0.33
BL	4.78 ± 0.91
CB	0 ± 0.33
CC	0 ± 0.17
CL	0 ± 0.22
LB	0.65 ± 0.53
LC	0 ± 0.14
LL	3.29 ± 0.82

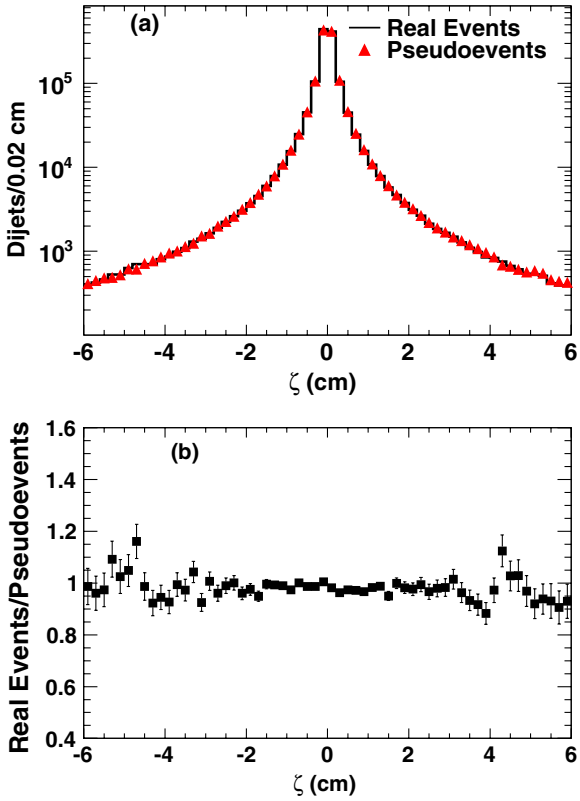

FIG. 7 (color online). The distribution of ζ for the real events (solid line) and pseudoevents (triangle points) in the control region (a), and their ratio (b).

performed on the three-dimensional histogram where the PDF information is stored. Random u, v, and α are chosen according to the PDF's distribution and assigned to the pseudojet.

To complete the process, a pseudoevent is generated for each event in the ZBB trigger data (which are part of the control or signal regions), thereby creating "pseudodata" with the proportion of secondary vertices and the flavor composition derived from the ZBB trigger data, and the secondary vertex information corresponding to SM sources via the PDFs.

C. Validation

We use the control region to validate this algorithm. Because we expect the control region to be devoid of signal, we can compare the real dijet data to the pseudodijets generated to see if the pseudoevent generation replicates the data. For the purposes of this validation, exactly one pseudoevent is generated for each real event, and the PDFs are only sampled once for each pseudojet. Distributions of the control region pseudoevent vs real events show that the pseudoevent generation is well behaved. Figure 7 shows the distribution of ζ in the control region for real events and pseudoevents, along with the ratio of the two distributions.

VI. SIGNAL SEARCH

A. From pseudoevents to a background estimate

To generate the background estimate, we create pseudodata as described above for events in the signal region. We construct a "pseudoexperiment" by sampling from the PDFs for each dijet in the ZBB trigger sample. We carry out this procedure 10 000 times to create an ensemble of pseudoexperiments. Each is treated independently and is passed through the same set of analysis cuts, which will be described in further detail. The resulting number of events that pass these cuts is calculated for each pseudoexperiment. The background estimate is the mean number of events that pass these cuts averaged over all pseudoexperiments and represents the number of events in ZBB trigger data that would pass the analysis cuts if only SM processes contributed to the observed data. We perform a simple counting experiment by comparing this background estimate to the number of observed data events with the same analysis cuts.

B. Signal to background optimization

To conduct our search, we investigate the following variables, optimizing the last three.

(1) $|d_0|_{\max}$ cut on tracks that are used by the tagging algorithm.
(2) Separation of the two jets (ΔR).
(3) ψ, the impact parameter of a tagged jet.
(4) ζ, the decay distance of the HV particle.

The $|d_0|_{\max}$ cut is a parameter of the tagging algorithm. Figure 8 shows the behavior of the signal MC simulation and background pseudodata, where one pseudoevent is generated for each real event, respectively, for the 20 $|d_0|_{\max}$ cuts investigated. The standard CDF $|d_0|_{\max}$ cut ($|d_0|_{\max} < 0.15$ cm) reduces the efficiency of finding secondary vertices from the signal MC events by more than half.

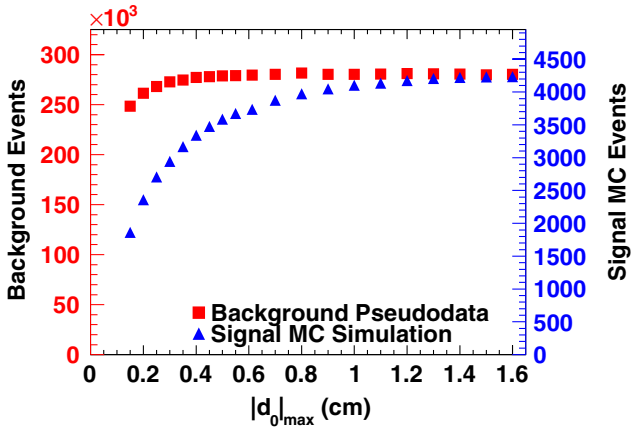

FIG. 8 (color online). Number of signal MC simulation events (triangle points) and background pseudoevents (square points) vs the b-tagging algorithm cut $|d_0|_{\max}$.

The distribution for the signal shows that larger $|d_0|_{\max}$ cuts allow for more signal acceptance, while the background plateaus at about $|d_0|_{\max} = 0.70$ cm. We choose the maximum $|d_0|_{\max}$ cut consistent with the physical constraints of the CDF detector. The inner detector contains a beam pipe with radius $r = 1.26$ cm. Attached to the beam pipe is a single layer of silicon strips, Layer00 (L00). While it is not required that tracks deposit hits in this innermost layer, we want to ensure that tracks originating from the primary vertex *could* hit this detector. Thus, the d_0 of tracks originating from a primary vertex must be less than the radius of the beam pipe. However, the beam line at CDF is not at the exact center of the detector. Accounting for this shift, we determine that tracks with a maximum $|d_0| < 1.0$ cm may deposit hits in L00, thus a $|d_0|_{\max} < 1.0$ cm is chosen.

With the $|d_0|_{\max}$ cut set, we optimize the cuts on the other three variables by maximizing $S/\sqrt{B}$. The cuts chosen for the low and high-HV-mass searches (20 GeV/c^2 for the former; 40 and 65 GeV/c^2 for the latter) are shown in Table IV. The searches are optimized separately because the low-mass HV results in daughter jets that are more collinear. This changes the nature of the ΔR cut. For the low-HV-mass search, only a $\Delta R_{\max} < 0.75$ cut is imposed; no $\Delta R_{\min}$ cut is applied.

An additional cut shown in Table IV is imposed on ζ. The magnitude of ζ must be less than the distance from the primary vertex to the closest secondary vertex. This ensures that the decay point is between the primary vertex and both secondary vertices.

An unanticipated source of background became apparent when we applied these analysis cuts to the real ZBB trigger events. A few events in the low-HV mass sample appear to contain a single secondary vertex from a B hadron in which some of the decay products are found in each of two nearby jet cones. This is a consequence of the small cone size used in the jet algorithm. Since this is a physical background that we had not thought of, we went to the signal MC to find criteria that would remove this source of background but not adversely affect the signal sensitivity. Two features of this background are that 1) the two secondary vertices have very small separation in the transverse plane (ΔS_{2d}), and 2) the total invariant mass of all the tracks in both vertices (Σm_{vtx}) is less than the b-quark mass. Table V shows the cuts made in these variables. When these cuts are added to the low-HV-mass search, the excess background described above is removed, while the reduction in the efficiency in the signal MC simulation is negligible.

TABLE IV. Variable cuts for both the low- and high-HV-mass searches.

Variable	high HV mass	low HV mass
$\lvert d_0\rvert_{\max}$ (cm)	<1.0	<1.0
$\Delta R_{\min}$	>0.75	n.a.
$\Delta R_{\max}$	<2.0	<0.75
$\lvert\psi\rvert$ (both jets) (cm)	>0.11	>0.12
ζ (cm)	>0.8	>0.7
$\lvert\zeta\rvert$ (cm)	$<$ Minimum(L_{xy1}, L_{xy2})	

TABLE V. Additional requirements on the low-HV-mass search due to an unanticipated background.

Variable	low HV mass
ΔS_{2d} (cm)	>0.06
OR	
Σm_{vtx} (GeV/c^2)	>5.0

C. Results

With the variable cuts set, we run 10 000 pseudoexperiments for both mass searches to estimate the SM background. The distributions of the number of pseudoevents passing the analysis cuts are Poisson distributions with means $\mu_{\text{low}} = 0.58$ and $\mu_{\text{high}} = 0.29$. The statistical uncertainties on these numbers are negligible. The systematic uncertainty due to the background estimate procedure is described in the next section.

With the same variable cuts, we can also calculate the number of expected signal MC events that we would obtain with the same integrated luminosity as the ZBB trigger. This is done by calculating the number of events that pass the cuts in each signal MC sample and multiplying this number by a scale factor consisting of the luminosity of the ZBB trigger sample multiplied by the cross section for Higgs boson production ($gg \rightarrow H$) divided by the number of signal MC events generated. The Higgs boson cross sections are obtained from Ref. [22]. For $M_H = 130$ GeV/c^2, the cross section is $\sigma_{gg\rightarrow H} = 858$ fb, while for $M_H = 170$ GeV/c^2, the cross section is $\sigma_{gg\rightarrow H} = 349$ fb. The branching ratio of the Higgs boson is assumed to be 100% to the HV particles, and the branching ratio of the HV particles is assumed to be 100% to $b\bar{b}$ pairs.

When calculating the expected number of signal MC, two reweightings are performed in order to account for differences between the ZBB trigger data and signal MC events. First, we reweight to account for differences in the luminosity profile of the signal MC events vs data events. The distribution of the number of primary vertices in data is divided by the same distribution in the MC events. The ratio is used as an event-by-event weight, ranging from 0.75 to 5.0 depending on the number of primary vertices, in order to match the luminosity profile of the signal MC simulation to the ZBB trigger data.

A second reweighting is performed to account for different trigger efficiencies for different run ranges in order to match the data's trigger efficiency to that of the signal MC simulation.

To account for the differences between the MC and data tagging efficiencies, a tagging scale factor for the tagging

TABLE VI. Results of the search. Two events remain after all cuts: one event in the low-HV-mass search, the second (different event) in the high-HV-mass search. Uncertainties are discussed in Sec. VII.

Higgs Boson Mass (GeV/c^2)	HV Mass (GeV/c^2)	HV lifetime (cm)	Expected Signal MC	Background Estimate	Number Observed
low-HV-mass search					
130	20	1.0	0.64	0.58	1
170	20	1.0	0.074	0.58	1
high-HV-mass search					
130	40	1.0	0.26	0.29	1
170	40	1.0	0.38	0.29	1
170	65	1.0	0.14	0.29	1
130	40	0.3	0.24	0.29	1
130	40	2.5	0.10	0.29	1
130	40	5.0	0.043	0.29	1

algorithm with $|d_0|_{\max} < 1.0$ cm is also applied twice ($SF_{\text{tagging}} = 0.9 \times 0.9 = 0.81$), because we have two tagged jets [5].

Finally, a scale factor ($SF_{\text{trigger}} = 1.12 \pm 0.11$) is applied to account for systematic effects present in the ZBB trigger simulation used on the signal MC events [18].

Table VI shows the results of our search. The number of expected signal events is calculated from each of the signal MC samples. The number of background events is also shown. Both uncertainties are calculated in the next section. Of the 6.2×10^6 data events in the signal region, 124 000 of which have two tagged jets, one event passes the analysis cuts in the low-HV mass search, and one different event passes these cuts in the high-HV mass search.

VII. SYSTEMATIC UNCERTAINTIES

The systematic uncertainties in this analysis fall into two main categories. The first are systematic effects that affect the background estimate. The second are the systematic effects that affect the number of expected signal MC events.

In the first category, there are three major sources of uncertainty, each corresponding to a step in the pseudoevent generation. First, the tagging probability is shifted by its statistical uncertainty one sigma in each direction. The results are propagated through as a systematic uncertainty.

The flavor composition probabilities used to determine the pseudoflavor of the jets result in two more systematic uncertainties: the statistical uncertainty from the flavor composition fractional fit and a systematic due to the MC simulation over-efficiency in track reconstruction, which has a direct impact on the vertex mass of the secondary vertex. When additional tracks in the MC are reconstructed, they will add to the vertex mass of the secondary vertex. For the former, we use one sigma shifts in both directions. For the latter, we use an overall 3% reduction in the vertex mass to model a maximal variation this over-efficiency would produce [23]. This reduction changes the flavor composition and propagates through as a systematic uncertainty.

We generate five new ensembles of pseudoevents where each is generated with one of the systematic shifts described above. For each, we perform another 10 000 pseudoexperiments as before and compare the background estimate to the central value calculated in Table VI. The percent difference is taken as the systematic uncertainty.

For the last of the three steps in pseudoevent generation, the PDF sampling, we turn to the bootstrap technique [24]. The bootstrap technique measures the systematic uncertainty arising from shape uncertainties in the PDFs. Effectively, the three-dimensional histograms are statistically varied within their Poisson statistical fluctuations, and a new background estimate is calculated using 10 000 new pseudoexperiments. This procedure is itself replicated 200 times. The standard deviation of these 200 means is the uncertainty associated with the PDF sampling.

The second category of systematic uncertainties affects the signal estimate. These include uncertainties associated with:

(1) jet energy scale,
(2) trigger simulation,
(3) tagging scale factor,
(4) parton distribution function,
(5) luminosity.

The first systematic uncertainty is calculated separately for each signal MC sample, while the systematic uncertainties on the trigger simulation, tagging scale factor, and luminosity have the same value across all samples, and the parton distribution function has approximately the same value for all samples.

The JES factor on jets is varied up (down) one sigma with respect to its central value. The result is that more (less) jets pass the $E_T^{\text{cor}} > 20$ GeV cut. This affects the

TABLE VII. Summary of systematic uncertainties for the background estimate and signal MC simulation. The JES is calculated separately for each signal MC sample.

Uncertainty	Down (%)	Up (%)
Background estimate—low-HV-mass search		
Data statistics	±0.039	
Tag probability statistics	−7.7	3.4
Flavor composition	−0.5	2.75
Background estimate—high-HV-mass search		
Data statistics	±0.046	
Tag prob. statistics	±3.9	
Flavor composition	−0.5	8.9
Signal MC		
Jet Energy Scale	−15.6 to −6.3	4.0 to 25.5
Trigger Uncertainty	±8.9	
Tagging scale factor	±10	
PDF	±2.5	
Luminosity	±6	

TABLE VIII. Null hypothesis p-values for this search.

Higgs Boson Mass (GeV/c^2)	HV Mass (GeV/c^2)	HV lifetime (cm)	p-value
low-HV-mass search			
130	20	1.0	0.44
170	20	1.0	0.43
high-HV-mass search			
130	40	1.0	0.27
170	40	1.0	0.26
170	65	1.0	0.26
130	40	0.3	0.27
130	40	2.5	0.27
130	40	5.0	0.27

number of expected signal MC events differently for each sample.

The ZBB trigger simulation scale factor has an uncertainty of 8.9%. The scale factor systematic uncertainty for the tagging algorithm at the operating point, $|d_0|_{\max} < 1.0$ cm, is 10%. The parton distribution function uncertainty is taken from Ref. [22] which documents this uncertainty for multiple analyses, including ones that use $gg \rightarrow H$ production (2.5%). Finally, the luminosity uncertainty is 6% [25].

All the systematic uncertainties calculated are shown in Table VII. These systematic uncertainties are used in the calculation of the limits discussed in Sec. VIII.

VIII. FINAL RESULTS AND CONCLUSION

With all the uncertainties calculated, we form test hypotheses consisting of our background estimate along with our signal MC. A separate test hypothesis is constructed for each set of masses and lifetimes. We also create corresponding null hypotheses consisting only of the background estimate for each HV mass search. Table VIII shows p-values for each set of masses, showing the probability that the null hypothesis has fluctuated to the data.

We do not observe a statistically significant excess, thus we proceed to set a limit on the production cross section times branching ratio of the HV model for the particular masses and lifetimes we studied. A Bayesian limit calculator is used for this calculation [26,27]. Table IX shows the resulting observed limit and median expected limit, along with the ±1 and ±2 sigma values on the expected limit, all at 95% confidence level (C.L.).

The counting experiment is performed with a small discrete number of events, where the background estimate is less than one. Thus, the expected number of events can only fluctuate up (from zero). The result is that the negative sigma expected limits are identical to the median limit.

TABLE IX. Observed and expected limits at 95% C.L. calculated for different signal MC samples.

Higgs Boson Mass (GeV/c^2)	HV Mass (GeV/c^2)	HV lifetime (cm)	Observed Limit (pb)	Expected Limit (pb)				
				-2σ	-1σ	median	$+1\sigma$	$+2\sigma$
			low-HV-mass search					
130	20	1.0	6.2	4.3	4.3	4.3	6.2	8.4
170	20	1.0	22.1	15.2	15.2	15.2	22.1	29.9
			high-HV-mass search					
130	40	1.0	15.9	10.5	10.5	10.5	15.9	21.5
170	40	1.0	4.4	2.9	2.9	2.9	4.4	6.0
170	65	1.0	11.7	7.7	7.7	7.7	11.7	15.7
130	40	0.3	17.8	11.7	11.7	11.7	17.8	24.2
130	40	2.5	40.7	26.8	26.8	26.8	40.7	55.1
130	40	5.0	94.3	62.0	62.0	62.0	94.3	127.9

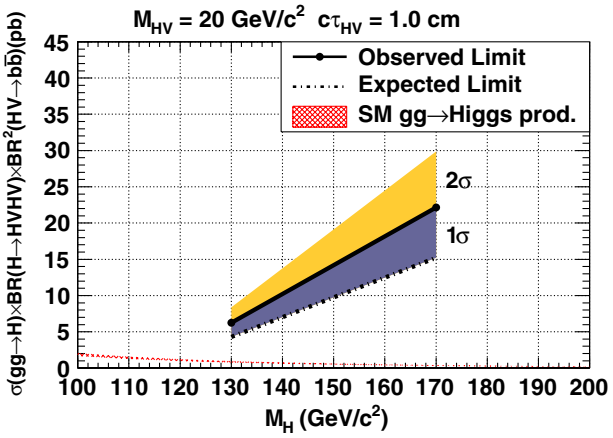

FIG. 9 (color online). Observed and expected limits at 95% C.L. with +1 and $+2\sigma$ bands for signal MC simulation with HV mass 20 GeV/c^2. The hashed line is the Higgs boson production cross section in the SM.

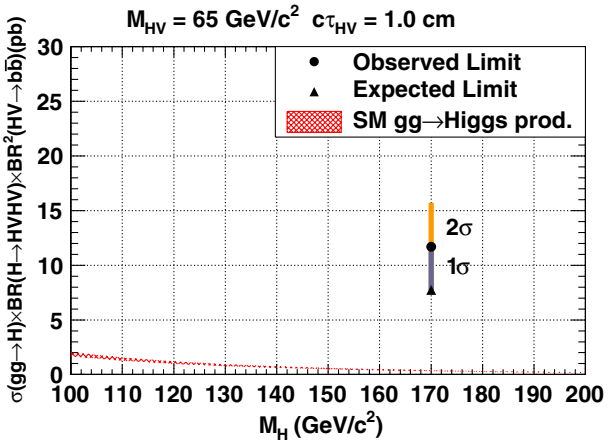

FIG. 11 (color online). Observed and expected limits at 95% C.L. with +1 and $+2\sigma$ bands for signal MC with HV masses 65 GeV/c^2. The hashed line is the Higgs boson production cross section in the SM.

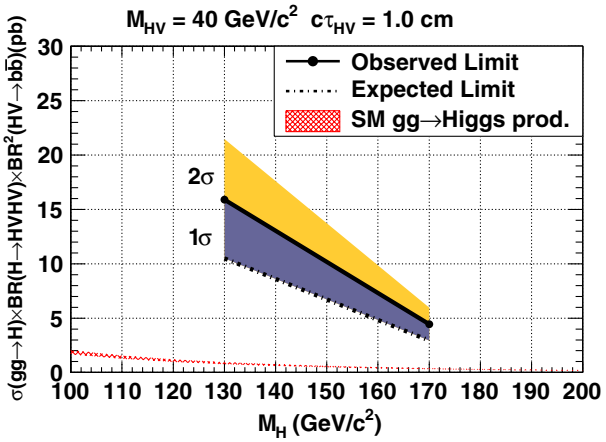

FIG. 10 (color online). Observed and expected limits at 95% C.L. with +1 and $+2\sigma$ bands for signal MC with HV masses 40 GeV/c^2. The hashed line is the Higgs boson production cross section in the SM.

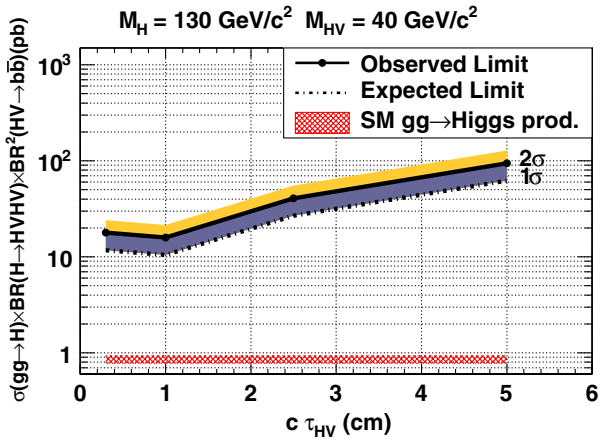

FIG. 12 (color online). Observed and expected limits at 95% C.L with +1 and 2σ bands for signal MC for differing HV particle lifetimes. The hashed line is the Higgs boson production cross section in the SM.

Also, the +1 sigma expectation is 1 event, which is what we see. Thus, our limit is the same as the +1 sigma expectation.

Figures 9–12 show the results of the limit calculation. In Figs. 9–11, the x-axis is the mass of the Higgs boson. Figure 9 is for a M_{HV} of 20 GeV/c^2 corresponding to the low-HV-mass search. Figure 10 is for a M_{HV} of 40 GeV/c^2, corresponding to the high-HV-mass search. Figure 11 shows the results of the high-HV-mass search for a M_{HV} of 65 GeV/c^2. Figure 12 shows the limits for M_H of 130 GeV/c^2 and M_{HV} of 40 GeV/c^2 with the HV lifetime on the x-axis.

In conclusion, we have searched for heavy metastable particles that decay into a jet pair at a displaced vertex at CDF. No statistically significant excess is observed, and limits are set on the production cross section times branching ratio for the HV phenomenology we have used as a benchmark. The results shown for this phenomenology can be used to constrain other models by considering the differences of the cross section, branching ratio, and the kinematics of the final state.

ACKNOWLEDGMENTS

We thank the Fermilab staff and the technical staffs of the participating institutions for their vital contributions. This work was supported by the U.S. Department of Energy and National Science Foundation; the Italian Istituto Nazionale di Fisica Nucleare; the Ministry of Education, Culture, Sports, Science and Technology of Japan; the Natural Sciences and Engineering Research Council of Canada;

the National Science Council of the Republic of China; the Swiss National Science Foundation; the A. P. Sloan Foundation; the Bundesministerium für Bildung und Forschung, Germany; the World Class University Program, the National Research Foundation of Korea; the Science and Technology Facilities Council and the Royal Society, UK; the Institut National de Physique Nucleaire et Physique des Particules/CNRS; the Russian Foundation for Basic Research; the Ministerio de Ciencia e Innovación, and Programa Consolider-Ingenio 2010, Spain; the Slovak R&D Agency; and the Academy of Finland.

[1] M. Strassler and K. Zurek, Phys. Lett. B **651**, 374 (2007).
[2] V. M. Abazov *et al.*, Int. J. Mod. Phys. A **20**, 3263 (2005).
[3] A. Bardi *et al.*, Nucl. Instrum. Methods A **409**, No. 1-3, 658 (1998).
[4] J. A. Adelman *et al.* (CDF Collaboration), Nucl. Instrum. Methods A **572**, No. 1, 361 (2007).
[5] F. Abe *et al.*, Nucl. Instrum. Methods **271**, 387 (1988); D. E. Acosta *et al.* (CDF Collaboration), Phys. Rev. D **71**, 052003 (2005); The CDF II Detector Technical Design Report No. Fermilab-Pub-96/390-E.
[6] A. Sill *et al.*, Nucl. Instrum. Methods A **447**, No. 1-2, 1 (2000); A. Affolder *et al.*, Nucl. Instrum. Methods A **453**, No. 1-2, 84 (2000); C. S. Hill *et al.*, Nucl. Instrum. Methods A **530**, 1 (2000).
[7] A. Affolder *et al.*, Nucl. Instrum. Methods A **526**, No. 3, 249 (2004).
[8] The CDF II uses a cylindrical coordinate system in which ϕ is the azimuthal angle, r is the radius from the nominal beamline, and z points in the proton beam direction. The transverse plane, $r-\phi$ plane, or sometimes referred to as x–y plane, is the plane perpendicular to the z axis. In addition, θ is defined as the polar angle measured with respect to the interaction vertex. Transverse momentum and energy are the projections of total momentum and energy onto the $r-\phi$ plane and defined as $p_T = p\sin\theta$ and $E_T = E\sin\theta$, respectively.
[9] L. Balka *et al.*, Nucl. Instrum. Methods A **267**, No. 2-3, 272 (1988); S. R. Hahn *et al.*, Nucl. Instrum. Methods A **267**, No. 2-3, 351 (1988).
[10] S. Bertolucci *et al.*, Nucl. Instrum. Methods A **267**, No. 2-3, 301 (1988); M. Albrow *et al.*, Nucl. Instrum. Methods A **480**, No. 2-3, 524 (2002); G. Apollinari *et al.*, Nucl. Instrum. Methods A **412**, No. 2-3, 515 (1998).
[11] S. Kuhlmann *et al.*, Nucl. Instrum. Methods A **518**, No. 1-2, 39 (2004).
[12] F. Abe *et al.* (CDF Collaboration), Phys. Rev. D **45**, 1448 (1992).
[13] D. Acosta *et al.*, Nucl. Instrum. Methods A **494**, No. 1-3, 57 (2002); M. Strassler and K. Zurek, Phys. Lett. B **651**, 374 (2007).
[14] M. Strassler and K. Zurek, Phys. Lett. B **661**, 263 (2008).
[15] D. Kaplan, M. Luty, and K. Zurek, Phys. Rev. D **79**, 115016 (2009).
[16] T. Sjöstrand, P. Edén, C. Friberg, L. Lönnblad, G. Miu, S. Mrenna, and E. Norrbin, Comput. Phys. Commun. **135**, 238 (2001).The version of PYTHIA used here is 6.216.
[17] E. Gerchtein and M. Paulini, in 2003 Conference for Computing in High-Energy and Nuclear Physics (CHEP 03), La Jolla, California, 2003, p. TUMT005.The version of GEANT used here is Report No. 3.21/14, see CERN Program Library Long Writeup W5013.
[18] J. Donini *et al.*, Nucl. Instrum. Methods A **596**, No. 3, 354 (2008).
[19] A. Bhatti *et al.*, Nucl. Instrum. Methods A **566**, No. 2, 375 (2006).
[20] D. E. Acosta *et al.* (CDF Collaboration), Phys. Rev. D **71**, 052003 (2005); C. Neu, Report No. FERMILAB-CONF-06-162-E.
[21] W. Verkerke and D. Kirkby (unpublished). For documentation and source code, see http://roofit.sourceforge.net and arXiv:physics/0306116.
[22] (The TEVNPH Working Group CDF, and D0 Collaborations), arXiv:1007.4587.
[23] T. Aaltonen *et al.* (CDF Collaboration), Phys. Rev. D **80**, 052003 (2009).
[24] B. Efron and R. J. Tibshirani, *An Introduction to the Bootstrap* (Chapman & Hall, New York, 1993).
[25] D. Acosta *et al.* (CDF Collaboration), Phys. Rev. Lett. **94**, 091803 (2005).
[26] T. Junk, Nucl. Instrum. Methods A **434**, No. 2-3, 435 (1999).
[27] K. Nakamura *et al.* (Particle Data Group), J. Phys. G **37**, 075021 (2010).